



Self-regulating passive fuel supply for small direct methanol fuel cells operating in all orientations

N. Paust^{a,*}, S. Krumbholz^b, S. Munt^a, C. Müller^c, P. Koltay^a, R. Zengerle^a, C. Ziegler^a

^a Laboratory for MEMS Applications, Department of Microsystems Engineering (IMTEK), University of Freiburg, Georges-Koehler-Allee 106, D-79110 Freiburg, Germany

^b Fraunhofer IZM, Gustav-Meyer-Allee 25, 13355 Berlin, Germany

^c Laboratory for Process Technology, Department of Microsystems Engineering (IMTEK), University of Freiburg, Georges-Koehler-Allee 103, D-79110 Freiburg, Germany

ARTICLE INFO

Article history:

Received 9 January 2009

Received in revised form 6 March 2009

Accepted 15 March 2009

Available online 26 March 2009

Keywords:

Passive DMFC

Self-regulating fuel supply

Capillary-force-driven bubble pump

ABSTRACT

A microfluidic fuel supply concept for passive and portable direct methanol fuel cells (DMFCs) that operates in all spatial orientations is presented. The concept has been proven by fabricating and testing a passive DMFC prototype. Methanol transport at the anode is propelled by the surface energy of deformed carbon dioxide bubbles, generated as a reaction product during DMFC operation. The experimental study reveals that in any orientation, the proposed pumping mechanism transports at least 3.5 times more methanol to the reactive area of the DMFC than the stoichiometry of the methanol oxidation would require to sustain DMFC operation. Additionally, the flow rates closely follow the applied electric load; hence the pumping mechanism is self-regulating. Oxygen is supplied to the cathode by diffusion and the reaction product water is transported out of the fuel cell along a continuous capillary pressure gradient. Results are presented that demonstrate the continuous passive operation for more than 40 h at ambient temperature with a power output of $p = 4 \text{ mW cm}^{-2}$ in the preferred vertical orientation and of $p = 3.2 \text{ mW cm}^{-2}$ in the least favorable horizontal orientation with the anode facing downwards.

© 2009 Elsevier B.V. All rights reserved.

1. Introduction

Direct methanol fuel cells (DMFCs) still attract a considerable amount of interest among researchers and scientists because of their high theoretical energy density and the comparatively easy handling. The recently proposed passive concepts for fueling DMFCs [1–11] are promising. These concepts aim to supply the fuel cell with reactants without the need for any external pumps and valves. The DMFC system becomes small and compact and the overall energy density is increased, which makes the DMFC attractive as a possible power source for portable electronic devices. However, in particular for the passive DMFC, the dependence of the performance on the spatial orientation of the DMFC poses a significant challenge. Both at the anode and the cathode, two-phase flow occurs which is subject to buoyancy effects at the anode and gravity at the cathode. Therefore, transport of the reaction products and educts strongly depends on the spatial orientation of the fuel cell. Whereas buoyancy forces can be used to drive a passive fuel supply in DMFCs with a fixed orientation [2], these effects are undesirable for the portable orientation-independent DMFC as demonstrated in [3]: An in-house fabricated DMFC breathes air at the cathode and has the methanol reservoir directly attached to the anode flow field. In

particular, the DMFC shows a rapid decline in performance for the horizontal orientation with the anode facing downwards, which is probably caused by CO_2 gas bubbles hindering the methanol supply at the anode and by water flooding the cathode. In [5], a brief overview is given of the existing concepts for passive DMFC operation and a new passive fuel management system is introduced. This system utilizes porous media for methanol fuel dosage and delivery. Due to the small dimensions in the porous media, surface forces dominate over volume forces, so the system is potentially independent of its orientation. However, the dependence of the performance on the orientation of the DMFC is not further discussed. In particular, the transport of CO_2 away from the porous medium out of the system remains unclear. In [10], a DMFC prototype is presented with a passive methanol dosage feature. A reservoir with pure methanol is separated from the flow field containing diluted methanol by a Teflon® membrane and the dosage of methanol is regulated by the concentration gradient of methanol across the membrane. The transport of methanol to the reactive area is dominated by diffusion and the reaction product carbon dioxide is transported by buoyancy forces to a hole where the CO_2 gas is vented. As the CO_2 transport is driven by buoyancy forces, the performance of the system depends on the orientation of the DMFC. Nevertheless, the fuel dosage system is promising because highly concentrated methanol is stored in the fuel tank which increases the energy density in comparison to the storage of diluted methanol.

* Corresponding author. Tel.: +49 761 2037313; fax: +49 761 2037322.
E-mail address: nils.paust@imtek.de (N. Paust).

Nomenclature

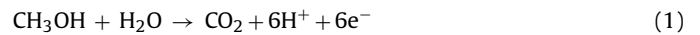
A_{MEA}	active area of the Membrane Electrode Assembly (MEA) (cm^2)
C_f	concentration of the aqueous methanol solution (mol m^{-3})
d	diameter of the poles of the bubble fence (mm)
D_{gap}	depth of the gaps between the poles of the bubble fence (mm)
F	Faraday constant ($F = 96485 \text{ C mol}^{-1}$)
g	acceleration due to gravity (9.81 m s^{-2})
h_1	channel height at the cathode side facing the MEA (mm)
h_2	channel height at the cathode side away from the MEA (mm)
h_b	channel height at the bubble's back meniscus (mm)
h_f	channel height at the bubble's front meniscus (mm)
h_{gcc}	channel height of the gas collection channel (mm)
h_{hyd}	difference in hydrostatic height (mm)
i	current density (mA cm^{-2})
l	length of the channel (mm)
L_{bub}	length of a gas bubble (mm)
M_{CO_2}	molar weight of CO_2 $M_{\text{CO}_2} = 44 \text{ g mol}^{-1}$
Δp_{cap}	capillary pressure difference over a deformed gas bubble in a tapered channel (Pa)
Δp_{int}	capillary pressure difference across a single liquid-gas interface (Pa)
Δp_{buo}	pressure difference across a bubble caused by buoyancy (Pa)
p_{eff}	pumping efficiency defined as the ratio between the liquid flow rate induced by the moving bubbles to the bubbly gas flow rate (–)
p	power density (mW cm^{-2})
r	radius of a liquid/gas interface (mm)
t	time (s)
T	temperature ($^{\circ}\text{C}$)
w	channel width at the anode (mm)
w_1	channel width at the cathode on the side facing the MEA (mm)
w_2	channel width at the cathode on the side away from the MEA (mm)
w_{gap}	width of the gaps between the poles of the bubble fence (mm)
w_{gcc}	channel width of the gas collection channel (mm)
x	horizontal coordinate
y	vertical coordinate
α	opening angle of the tapered channel ($^{\circ}$)
θ	contact angle ($^{\circ}$)
θ_{hys}	contact angle hysteresis ($^{\circ}$)
θ_{ad}	advancing contact angle ($^{\circ}$)
θ_{rec}	receding contact angle ($^{\circ}$)
Φ	flow rate ($\mu\text{l min}^{-1}$)
κ	curvature of the liquid/gas interface (m^{-1})
ρ	fluid density (methanol solution 2M: $\rho_l = 968 \text{ kg m}^{-3}$; CO_2 gas: $\rho_g = 1.98 \text{ kg m}^{-3}$)
σ	surface tension (methanol solution 2M; $T = 23^{\circ}\text{C}$: 0.062 N m^{-1})

The main objective of our current work is to address the challenge of the orientation-independent performance of passive DMFCs. Fuel transport driven by capillary forces is used to implement a passive fuel supply in all spatial directions. The focus is on the supply mechanism to the anode where a passive CO_2 -bubble pump delivers methanol by convection in a similar way to an active

supply mechanism but without the need for any external components such as pumps or valves. The bubble pump utilizes the surface forces of deformed CO_2 bubbles in tapered channels and ensures CO_2 degassing and methanol supply regardless of the orientation of the fuel cell. Furthermore, the supply mechanism is fully self-regulating as the bubble generation frequency is proportional to the electric load. Additionally, a cathode flow field with water removal driven by capillary forces has been added to ensure stable passive DMFC performance. The flow field is made of micro-structured porous carbon in which oxygen is supplied by diffusion. The reaction product, water, is transported out of the DMFC along a continuous capillary gradient which prevents flooding of the cathode flow field.

2. Operating principle

In the present study, the DMFC is operated with a liquid water–methanol mixture at the anode and air at the cathode. The methanol oxidation reaction at the anode yields:



At the cathode, oxygen is reduced to water:



The proposed passive DMFC is depicted schematically in Fig. 1. The anode flow field consists of parallel tapered channels (Fig. 1 (part 2)). As soon as a CO_2 bubble that has grown on or emerged from the Porous Transport Layer (PTL) touches the upper and lower surfaces of the tapered channel, it becomes deformed, forming interfaces with different curvatures at the two ends of the bubble. As a result, a capillary pressure gradient is induced over the bubble that transports the bubble towards the greater cross-section of the tapered channel. Details of this mechanism including a discussion on the influence of geometric parameters and wetting properties, are presented in our previous work [12]. Each channel terminates at a gas collection channel that connects the parallel channels with each other. The gas collection channel is covered with a hydrophobic membrane (Fig. 1 (part 3)) such as that utilized in [13] for gas venting in a miniaturized bubble pump. The hydrophobic membrane allows the carbon dioxide to pass whereas the liquid is blocked. At the lower end of the gas collection channel, a bubble fence (Fig. 1 (part 4)) is embedded that allows the liquid to pass but blocks the gas. As a consequence, the bubbles moving along the

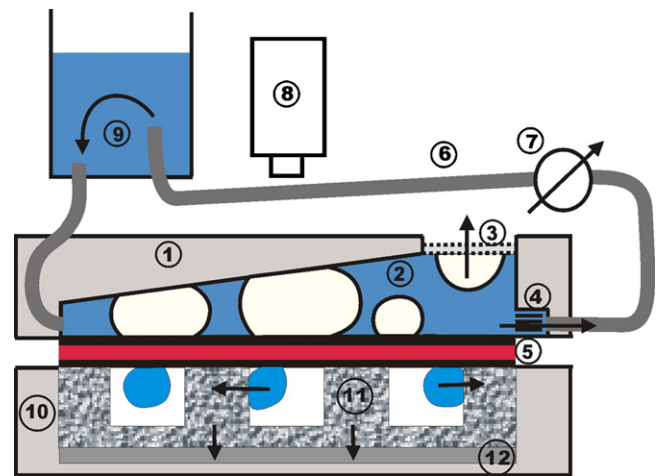


Fig. 1. Schematic of the passive DMFC. (1) Transparent anode flow field; (2) tapered channel; (3) hydrophobic membrane; (4) bubble fence; (5) PTL and MEA; (6) tubing; (7) flow sensor; (8) camera; (9) reservoir; (10) cathode mount; (11) cathode flow field; (12) non-woven material for capillary water transport.

tapered channels pump the methanol solution through the bubble fence and the tubing into the reservoir and leave the system through the hydrophobic membrane. Simultaneously, the bubble movement sucks liquid from the reservoir into the narrow end of the channel. Thus, a net circulation of methanol is induced that supplies the DMFC with methanol.

Fuel supply at the cathode is achieved by diffusion of oxygen in ambient air. For such an air-breathing DMFC, the accumulation of water in the cathode flow field creates significant difficulties [14]. In the current work, a micro-structured, hydrophilic, porous carbon flow field has been used that strongly draws water into the bulk material. Thus, oxygen diffusion through the channels is never blocked. Non-woven material with a higher capillarity than the porous carbon is attached to the carbon flow field in order to transport the water further out of the DMFC, where the water finally evaporates.

3. Design of the passive anode and cathode

Commercially available membrane electrode assemblies (MEAs) and porous transport layers (PTLs) have been used in the studied DMFC assemblies. Thus, the discussion is limited to the anode and cathode flow fields.

3.1. Anode flow field

In a first step, the main parameters for the anode flow field channels are approximated by a simple model to ensure that the capillary pressure of the bubbles is large enough to transport the bubbles along the channel even against their buoyancy forces. The bubbles are transported against buoyancy forces when the DMFC is oriented vertically with the opening of the tapered channels facing downwards. The maximum volume to surface force ratio and thus the maximum influence of buoyancy effects occurs when the bubble is at the channel outlet, just before it moves into the gas collection channel. This configuration is schematically depicted in Fig. 2. If the capillary pressure across the bubble of length L_{bub} at this position is large enough to move the bubble against buoyancy forces, any bubble of length L_{bub} or larger at any position in the tapered channel will be transported under any DMFC orientation by capillary forces to the hydrophobic membrane, where the bubble is vented. Thus, in this design step, the vertically oriented DMFC is considered, in which the buoyancy pressure Δp_{buo} and the capillary pressure Δp_{cap} are calculated for a bubble with its front meniscus situated at the end of the tapered channel at the intersection to the

gas collection channel:

$$\Delta p_{buo} = (\rho_f - \rho_g)gL_{bub} \quad (3)$$

$$\Delta p_{cap} = 2\sigma(\kappa_b - \kappa_f). \quad (4)$$

In Eq. (3), the bubble length L_{bub} is equivalent to the difference in hydrostatic height across the bubble, ρ_f is the density of the fluid, ρ_g is the density of the gas, and g is the acceleration due to gravity. The curvatures of the liquid/gas interfaces κ_b and κ_f at the back and the front of the bubble, respectively, can each be calculated from the two main curvatures arising in the top and side projection planes of the bubble, as further detailed in [15]. In the following, it is assumed that all gas bubbles which move through the channels of the vertically oriented DMFC touch all four channel surfaces. If the bubble moves towards the opening of the channel, the curvatures of the bubble interfaces yield:

$$\kappa_b = \cos\left(\theta_{ad} + \frac{\alpha}{2}\right) \frac{1}{h_b} + \cos(\theta_{ad}) \frac{1}{w} \quad (5)$$

$$\kappa_f = \cos\left(\theta_{rec} - \frac{\alpha}{2}\right) \frac{1}{h_f} + \cos(\theta_{rec}) \frac{1}{w}$$

In Eq. (5), the opening angle of the tapering is denoted by α , w is the channel width, and h_b and h_f are the channel heights at the position of the back and the front meniscus, respectively. θ_{ad} and θ_{rec} are the advancing and the receding contact angles which differ from each other due to the phenomenon of contact line pinning that causes a contact angle hysteresis as described in [16]: $\theta_{hys} = \theta_{ad} - \theta_{rec}$.

For a bubble moving backwards towards the inlet, i.e. when buoyancy forces exceed the capillary forces, the advancing meniscus becomes a receding one and vice versa. The curvatures of the interfaces are thus calculated by:

$$\kappa_b = \cos\left(\theta_{rec} + \frac{\alpha}{2}\right) \frac{1}{h_b} + \cos(\theta_{rec}) \frac{1}{w} \quad (6)$$

$$\kappa_f = \cos\left(\theta_{ad} - \frac{\alpha}{2}\right) \frac{1}{h_f} + \cos(\theta_{ad}) \frac{1}{w}$$

For the studied bubble position depicted in Fig. 2, the channel height at the front meniscus of the bubble h_f is the channel height at the intersection of the tapered channel and the gas collection channel. The channel height of the back meniscus can be calculated as a function of the bubble length as follows:

$$h_b = \frac{h_f - \tan(\alpha/2)(2L_{bub} - h_f \tan(1/4(\alpha + \pi - 2\theta_{rec})))}{1 - \tan(\alpha/2)\tan(1/4(-\alpha + \pi - 2\theta_{ad}))} \quad (7)$$

for a bubble moving in the pumping direction. If the bubble moves against the pumping direction, the channel height at the back meniscus yields:

$$h_b = \frac{h_f - \tan(\alpha/2)(2L_{bub} - h_f \tan(1/4(\alpha + \pi - 2\theta_{ad})))}{1 - \tan(\alpha/2)\tan(1/4(-\alpha + \pi - 2\theta_{rec}))} \quad (8)$$

If for a given bubble length L_{bub} the capillary pressure calculated with Eq. (4), Eq. (5), and Eq. (7) exceeds the pressure difference caused by buoyancy (Eq. (3)), the bubble moves towards the hydrophobic membrane. If the buoyancy pressure exceeds the capillary pressure calculated with Eq. (4), Eq. (6), and Eq. (8), the bubble moves backwards. If neither of the above statements is true, the bubble does not move. In this case, the difference between the buoyancy force and the capillary force is equalized by the pinning force that causes the contact angle hysteresis.

With the presented set of equations (Eqs. (3)–(8)), the geometric parameters and wetting properties of the tapered channels of the anode flow field can be determined so that the bubbles move in the preferred pumping direction even against buoyancy forces.

In a second step, the pump performance of the passive anode flow field is characterized. The focus is to analyze the liquid flow

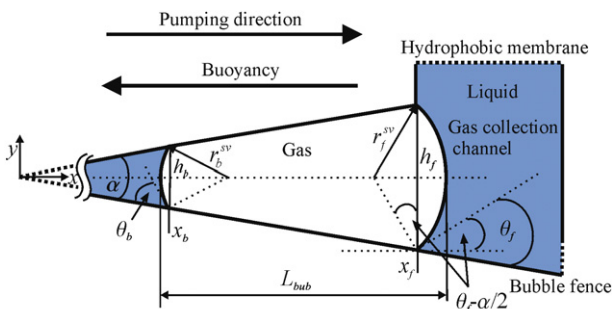


Fig. 2. Schematic of a gas bubble at the intersection of the tapered channel to the gas collection channel. The contact angles are specified as the front contact angle θ_f and the back contact angle θ_b with respect to the main pumping direction. If the bubble moves in the pumping direction, θ_f is the receding and θ_b the advancing contact angle. If the bubble moves against the main pumping direction, θ_f is the advancing and θ_b the receding contact angle. The indexes “sv” and “tv” stand for side view projection and top view projection, respectively. The curvature at the front and the back meniscus are calculated by $k = 0.5(r_{sv}^{-1} + r_{tv}^{-1})$ as shown in Eqs. (5) and (6).

rates induced by the moving bubbles for different DMFC orientations. The pumping efficiency p_{eff} , defined as the ratio of the induced liquid flow rate to the bubbly CO_2 gas flow rate is used to evaluate the pump performance of the anode flow field.

$$p_{eff} = \frac{\Phi_{liquid}}{\Phi_{gas}} \quad (9)$$

In our previous work [12], p_{eff} was studied for different channel types, channel geometries, and surface coatings in singly tapered channels with the gas flow supplied by a syringe pump. For the present study, the pump performance in the anode flow field consisting of six parallel channels is characterized during DMFC operation for different orientations of the DMFC. During passive operation, it is assumed that the liquid is saturated with CO_2 , so that all CO_2 is generated in the gaseous phase and the volumetric gas flow rate Φ_{gas} can be calculated from the current density i , the molar weight M_{CO_2} , the density ρ_{CO_2} and the active area of the MEA as follows:

$$\Phi_{gas} = \frac{A_{\text{MEA}} M_{\text{CO}_2} \cdot i}{\rho_{\text{CO}_2} 6F} \quad (10)$$

where F is the Faraday constant. For the operating DMFC, the minimum pumping efficiency to fulfill the stoichiometry requirements of the methanol oxidation reaction (MOR) yields:

$$p_{eff}^{\text{MOR}} = \frac{\rho_{\text{CO}_2}}{M_{\text{CO}_2} C_f} \quad (11)$$

where M_{CO_2} is the molecular weight of CO_2 and C_f is the molar concentration of the aqueous methanol solution. In the present work, a methanol concentration of the water–methanol solution that corresponds to 2 mol l^{-1} was used. Assuming the density of carbon dioxide at room temperature, the minimum required pumping efficiency for the MOR yields $p_{eff}^{\text{MOR}} = 2\%$. The actual p_{eff} at the anode flow field must be higher than the minimum value based on stoichiometry because of methanol crossover [17,18]. In [19], an equivalent methanol crossover current is reported to be several times higher than the actual electric current and in [8], the methanol crossover flow for a specific passive DMFC is estimated to 2.7 times higher than the methanol consumption by the MOR for a specific operation point. To account for the losses of methanol caused by crossover, the aim of this work is to design a passive supply mechanism as described in Section 2 that delivers methanol with a pumping efficiency that is at least 3 times but preferably more than 3 times higher than the p_{eff} of 2% required for the MOR.

3.2. Cathode flow field

The cathode flow field has been designed to match the geometry of the anode flow field. Parameters studied in advance were the capillarity of the porous carbon needed for the water transport and the channel cross-sections designed to ensure sufficient diffusive oxygen transport. The formation and removal of water droplets emerging from the PTL at the cathode of hydrogen-fueled Polymer Electrolyte Membrane (PEM) fuel cells is studied in [20]. In that study, contact angles on different porous carbon materials are reported to vary from $\theta = 125^\circ$ to $\theta = 145^\circ$. Such hydrophobic behavior is desired on the PTL because it prevents flooding but for the porous carbon flow fields the high contact angles would not allow for the proposed water removal mechanism. Therefore, the porous carbon of the cathode flow field was made hydrophilic by plasma activation. After the plasma treatment, a droplet touching the material is sucked into the bulk material as schematically depicted in Fig. 1. The average capillary pressure in the porous carbon was determined by dipping the flow field into water and measuring the hydrostatic height of the wetted material. A height of $h_{hyd} = 9.5 \text{ cm}$ was measured which corresponds to an average

capillary pressure of $\Delta p_{int} = \rho_{\text{H}_2\text{O}} g h_{hyd} = 932 \text{ N m}^{-2}$. A droplet emerging from the PTL and touching the side walls of the channel is sucked into the bulk material due to this capillary pressure caused by the wetting of the hydrophilic carbon material. During DMFC operation, more and more water accumulates in the porous flow field. As soon as the water reaches the sides of the flow field, it is further transported into the attached non-woven material, which exhibits an even higher capillary pressure of $\Delta p_{int} = 1033 \text{ N m}^{-2}$. From the non-woven material, the water evaporates to the environment. The carbon flow field is micro-structured with channels in order to ensure free diffusion paths in the flow field even if water accumulation partially blocks the pores of the porous carbon. The capillary water-transport mechanism in combination with an electro-osmotic pump has been used for water management in hydrogen-fueled PEM fuel cells [21]. To our knowledge, the application to fully passive DMFCs as described in the present paper is investigated here for the first time. As an initial approach, the same channel cross-sections as presented in [21] are used as detailed in the following section.

4. Experimental

An exploded view of the passive DMFC is depicted in Fig. 3. The Membrane Electrode Assembly (MEA) (catalyst-coated[®] Nafion N115; active area: $A_{\text{MEA}} = 2.6 \text{ cm}^2$; anode: 3 mg cm^{-2} PtRu; cathode: 1.3 mg cm^{-2} Pt manufactured by BalticFuelCells) is sandwiched between two PTLs, a $280 \mu\text{m}$ thick PTL (SGL, [®]SIGRACET GDL31-BA) at the anode that has been made hydrophilic by plasma activation and a hydrophobic PTL (SGL, [®]SIGRACET S10CC) with a microporous layer facing the MEA at the cathode.

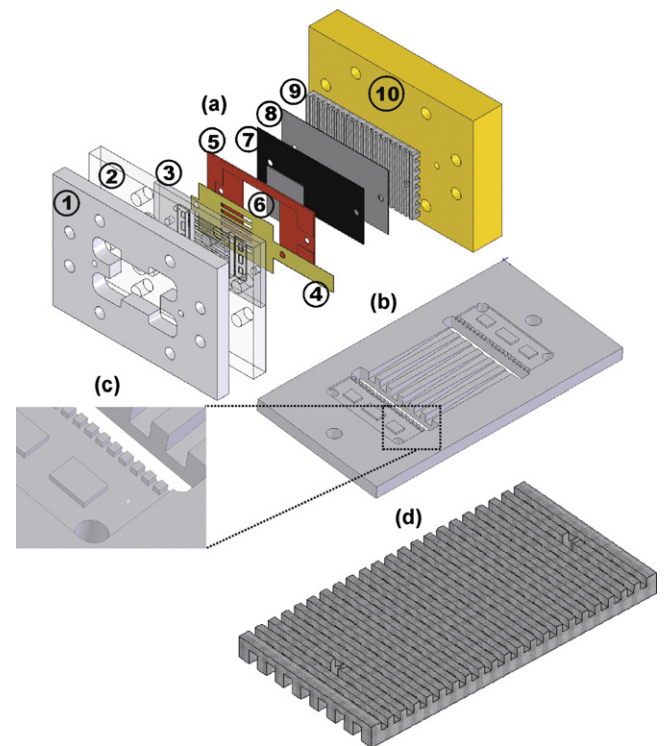


Fig. 3. (a) Exploded view of the passive DMFC system. (1) Aluminum support plate; (2) transparent end plate; (3) anode flow field; (4) current collector; (5) vacuum-cast PDMS sealing; (6) anode PTL; (7) MEA; (8) cathode PTL; (9) cathode flow field; (10) conductive end plate. (b) Enlarged anode flow field. (c) Enlarged section of the anode flow field showing the intersection of the tapered channels and the gas collection channel and the bubble fence. (d) Cathode flow field showing the channels on the side facing the MEA (upper surface) and the perpendicular channels on the side away from the MEA (lower surface).

The anode flow field consists of six parallel tapered channels fabricated by micro-milling in transparent COC. A detailed view of the flow field is given in Fig. 3 (b). Each channel has an inlet height of $h_{in} = 0.2$ mm, is $w = 1.2$ mm wide, has an opening angle of $\alpha = 4^\circ$ and is $l = 14.3$ mm long. The channels are coated with a hydrophilic polymer DMAAm–MaBP [22] by dip coating which results in contact angles of the water–methanol solution at the walls of $\theta = 10^\circ$. At the channel end, a gas collection channel with a cross-section of $h_{gcc} \cdot w_{gcc} = 2$ mm \cdot 2 mm connects the parallel channels with each other. In the gas collection channel, the CO₂ gas phase is separated from the liquid by a hydrophobic membrane (Fig. 1 (part 3)) (Whatman PTFE TE36) that enables gas venting but holds back the liquid by capillary forces and a bubble fence (Fig. 1 (part 4) and Fig. 3(c)) that allows the liquid phase to pass but retains the gas, again, by capillary forces. The bubble fence consists of 20 hydrophilic coated COC poles with a diameter of $d = 0.3$ mm separated by gaps of a width of $w_{gap} = 0.2$ mm as detailed in Fig. 3 (c). The gaps for transmitting the liquid have a depth of $D_{gap} = 0.2$ mm. The bubbles moving along the tapered channels pump the methanol solution through the bubble fence and the tubing into the reservoir and leave the system through the hydrophobic membrane. At the channel inlet, the same gas collection channel with the gas–liquid separation feature is added in order to avoid that small bubbles moving out of the inlet, driven for example by buoyancy forces in the vertical orientation, accumulate and subsequently block the channel inlets.

Since the flow field consists of non-conductive COC, a current collector is added (Fig. 3 (part 4)) that was manufactured by laser cutting of stainless steel and electroplated with a 5 μ m gold layer. The anode is sealed by a vacuum-cast PDMS layer (Fig. 3 (part 5)).

The cathode flow field is 3 mm thick and consists of porous carbon (SGL, PGP) (Fig. 1 (part 11) and Fig. 3 (d)) that was also made hydrophilic by plasma activation. Channels in the direction perpendicular to the methanol channels at the anode are milled into the carbon. The cross-section of these channels is $h_1 \cdot w_1 = 1$ mm \cdot 1 mm. In order to enhance the oxygen diffusion, channels with a cross-section of $h_2 \cdot w_2 = 2$ mm \cdot 1.5 mm are milled into the porous carbon on the side away from the MEA, in direction perpendicular to the channels on the side facing the MEA.

5. Results

5.1. Capillary forces, buoyancy forces and pinning

For the considered anode flow field, the movement of bubbles against buoyancy forces is analyzed with the set of equation introduced in Section 3.1 (Eqs. (3)–(8)). In Fig. 4, the difference between the capillary pressure and the buoyancy pressure of a bubble with its front meniscus situated at the channel outlet (see Fig. 2) is plotted as a function of the bubble length. The static contact angle of $\theta = 10^\circ$ measured on the polymer-coated COC for a 2 M methanol solution and the surface tension of a 2 M water methanol solution at room temperature ($\sigma = 0.062$ N m⁻¹) [24] are used for this analysis. A positive pressure difference means that the bubble moves in the pumping direction, a negative pressure difference means that the bubble moves backwards towards the narrower part of the channel and zero pressure indicates that the bubble pins to the channel walls. It can be seen that if no contact line pinning is assumed, a bubble longer than 8.5 mm would move in the pumping direction and a bubble smaller than 8.5 mm would move backwards. When it is assumed that contact line pinning can occur, bubbles of a certain length pin at the walls as indicated by a zero pressure difference in Fig. 4. For example, for a contact angle hysteresis of $\theta_{hys} = 20^\circ$, a bubble of a length shorter than 6.5 mm would move backwards against the pump direction, a bubble longer than the 6.5 mm but shorter than 9.9 mm would pin at the channel wall, and for bubbles longer

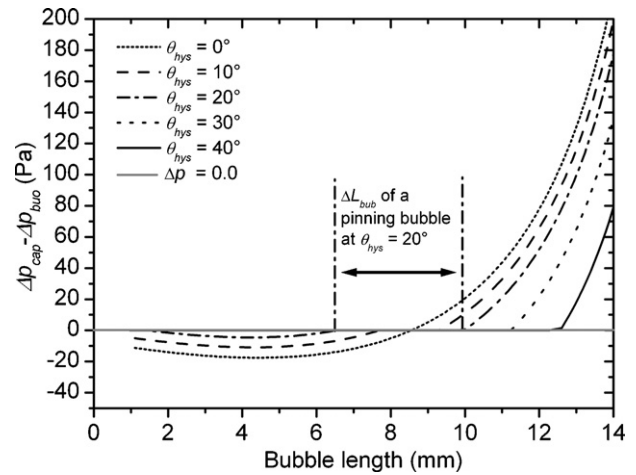


Fig. 4. Capillary pressure versus buoyancy pressure across a single bubble at the intersection of the tapered channel and the gas collection channel in a vertically oriented anode flow field (as depicted schematically in Fig. 2). The bubble is assumed to touch all four channel surfaces, so the smallest bubble length considered is 1.2 mm.

than 9.9 mm, the capillary pressure difference reduced by the contact angle hysteresis would exceed buoyancy pressure. For a contact angle hysteresis larger than $\theta_{hys} = 20^\circ$, the backward movement vanishes. In that case, the buoyancy forces are never large enough to move bubbles that fill the complete channel cross-section, no matter how long the bubbles are. However, bubble movement in the pumping direction still occurs. For a contact angle hysteresis of $\theta_{hys} = 30^\circ$, bubbles longer than $L_{bub} = 11.25$ mm move towards the hydrophobic membrane and for $\theta_{hys} = 40^\circ$, the bubble length must exceed $L_{bub} = 12.6$ mm. If the contact angle hysteresis is larger than $\theta_{hys} = 54^\circ$, the pumping mechanism fails because the bubbles would have to grow larger than the complete channel length in order that the capillary forces reduced by pinning would overcome buoyancy forces.

At temperatures higher than room temperature, the surface tension of the methanol solution decreases. Cell temperatures for the passive DMFC under passive conditions fed with a 2 M methanol solution have been reported to be up to 35 °C [6]. For active DMFCs, typical operation temperatures are around 85 °C [23]. The surface tension of water decreases from $\sigma_{H_2O}(23^\circ\text{C}) = 0.073$ N m⁻¹ at room temperature to $\sigma_{H_2O}(85^\circ\text{C}) = 0.062$ N m⁻¹ [24]. Assuming a similar decrease of the surface tension of the aqueous methanol solution, at 85 °C, the bubbles would have to grow somewhat larger so that the capillary forces reduced by pinning would overcome the buoyancy forces. For example, at a hysteresis of $\theta_{hys} = 20^\circ$ and a surface tension of $\sigma_{2M\text{MeOH}}(85^\circ\text{C}) \approx 0.053$ N m⁻¹, a bubble longer than 10.8 mm would move in pumping direction whereas for the surface tension at room temperature, the bubble would have to be larger than 9.9 mm. At $T = 85^\circ\text{C}$, for a hysteresis of $\theta_{hys} = 51^\circ$, the bubble length would have to exceed the channel length to be transported in pump direction whereas at room temperature, a hysteresis $\theta_{hys} = 54^\circ$ would be acceptable.

The result of this evaluation is that the passive anode moves gas bubble against the buoyancy forces as long as the contact angle hysteresis at the channel walls does not exceed $\theta_{hys} = 54^\circ$ at room temperature and $\theta_{hys} = 51^\circ$ at $T = 85^\circ\text{C}$. These hysteresis values that would cause the system to malfunction are much higher than the values that have been observed in the investigated anode flow fields even after an exposure of the samples to ambient air for more than three months. Therefore, at typical DMFC operation conditions, the proposed geometry is suitable for passive fuel supply even in vertically oriented DMFCs with bubbles moving against buoyancy forces.

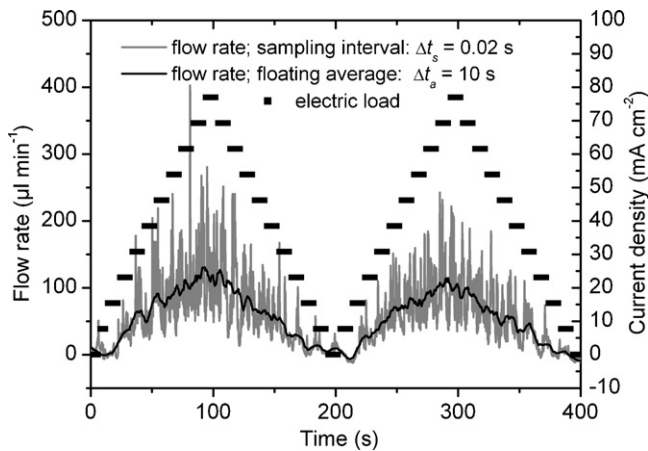


Fig. 5. Current density and flow rate plotted against time for two galvanostatic load cycles; $T = 23^\circ\text{C}$.

5.2. Pumping performance of the passive supply mechanism at the anode

The liquid flow rates induced by moving gas bubbles were studied during DMFC operation. Fig. 5 shows the liquid flow rate and the electric current density for two electric load cycles plotted against time. The load cycle was performed with galvanostatic steps ($\Delta t = 10\text{ s}$; $\Delta i = 7.7\text{ mA cm}^{-2}$) with the DMFC in a horizontal position at room temperature ($T = 23^\circ\text{C}$). The floating average with a time span of 10 s shows maxima and minima closely following the electric load. At the first peak, a pumping efficiency of $p_{\text{eff}} = 22\%$ was determined and for the second peak $p_{\text{eff}} = 20\%$. Considering the average current density and the average flow rate over the two complete cycles, the pumping efficiency yields $p_{\text{eff}} = 19\%$. In Fig. 6, a detail of Fig. 5 is plotted that shows the flow rates together with the pressure difference measured between the anode inlet and the anode outlet between $t = 200\text{ s}$ and $t = 250\text{ s}$. In this detail, the fluidic response to the electric current at the end of the first load cycle, at the transition to the second load cycle, and in the beginning of the second load cycle is depicted. It can be seen that the flow rate is closely related to the pressure difference, which is not surprising but proves that the flow rate fluctuations with each single peak are actually caused by single bubbles moving through the tapered channels and pumping the liquid water–methanol mixture and not by any other measurement noise.

The fluidic response to an electric load cycle starts with the nucleation of gas bubbles (beginning of the second cycle in Fig. 6;

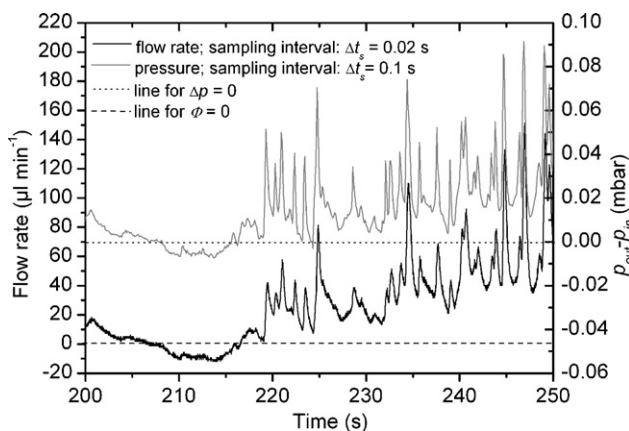


Fig. 6. Pressure difference between the outlet and the inlet of the anode flow field and the corresponding flow rate plotted against time for the end of the first and the beginning of the second load cycle depicted in Fig. 5.

$217\text{ s} \leq t \leq 219\text{ s}$). The gas bubbles displace liquid out of the flow field and the flow sensor, as arranged in the measurement set-up depicted in Fig. 1, shows a positive flow rate. In this initial state, liquid also flows out of the channel end with the smaller cross-section, thus, no net flow is generated in pump direction. As the growing bubbles touch both channel walls and the capillary pressure overcomes the resistance caused by contact line pinning, the bubbles start moving towards the increasing channel cross-section, and the actual pumping starts (Fig. 6; $t > 219\text{ s}$): the moving bubbles suck liquid into the narrow channel end and push liquid out of the channel end with the larger cross-section. At the end of a load cycle and in the beginning of the following load cycle until new gas bubbles are formed (Fig. 6; $207\text{ s} \leq t \leq 217\text{ s}$), the remaining gas in the gas collection channel continues to leave the flow field through the hydrophobic membrane. At this state again, no net flow in pump direction occurs. Liquid flows from the reservoir into the channel at both channel ends replacing the gas that leaves the system through the hydrophobic membrane, thus, the flow sensor as arranged in Fig. 1 shows negative flow rates.

Since the liquid flow rate closely follows the electric load, the methanol supply is regulated by the passive anode flow field. The response time is of the order of 10 s whereas a response time of several minutes would be sufficient due to the storage of methanol in the channel and the PTL. Thus, the anode is fully self-regulating and no external components are required to control the methanol supply.

In Fig. 7, the average pumping efficiency of the anode of the DMFC is plotted against the current density for different DMFC orientations. To extend the operation range of the current density, the DMFC was heated to 50°C for this experiment. Each data point was acquired by averaging the flow rates over 10 min and repeating the measurements 3 times on different days. The smallest p_{eff} was measured at a current density of $i = 13.5\text{ mA cm}^{-2}$ in a vertical position with the bubbles moving upwards driven by buoyancy forces (Fig. 7 light grey line). The reason for the small p_{eff} is the dominating non-blocking pumping mode in this configuration which can be understood as follows: As depicted in Fig. 8(a), comparatively small bubbles that do not fill the cross-section of the tapered channel move along the channel from the smaller to the larger cross-section, driven by buoyancy forces. As discussed in our previous work [12], in the non-blocking pumping mode, the major share of the liquid displaced by moving bubbles circulates directly around the bubbles and only a minor part contributes to the pumping mechanism. As the bubble generation frequency increases with

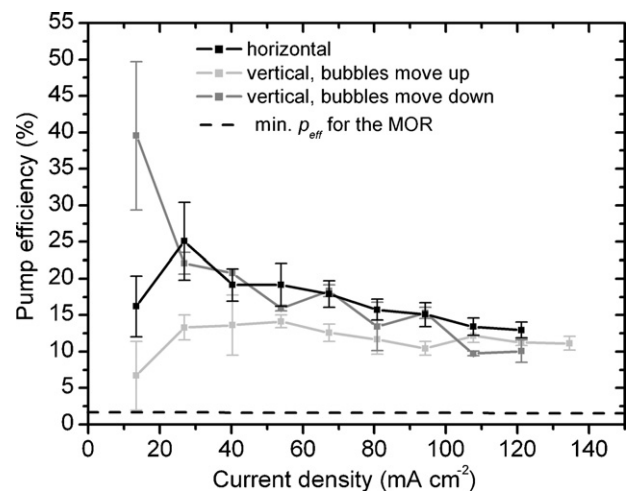


Fig. 7. Pumping efficiency of the passive anode flow field plotted against the current density for different DMFC orientations. The DMFC was heated to $T = 50^\circ\text{C}$ in order to extend the operation range of the current density.

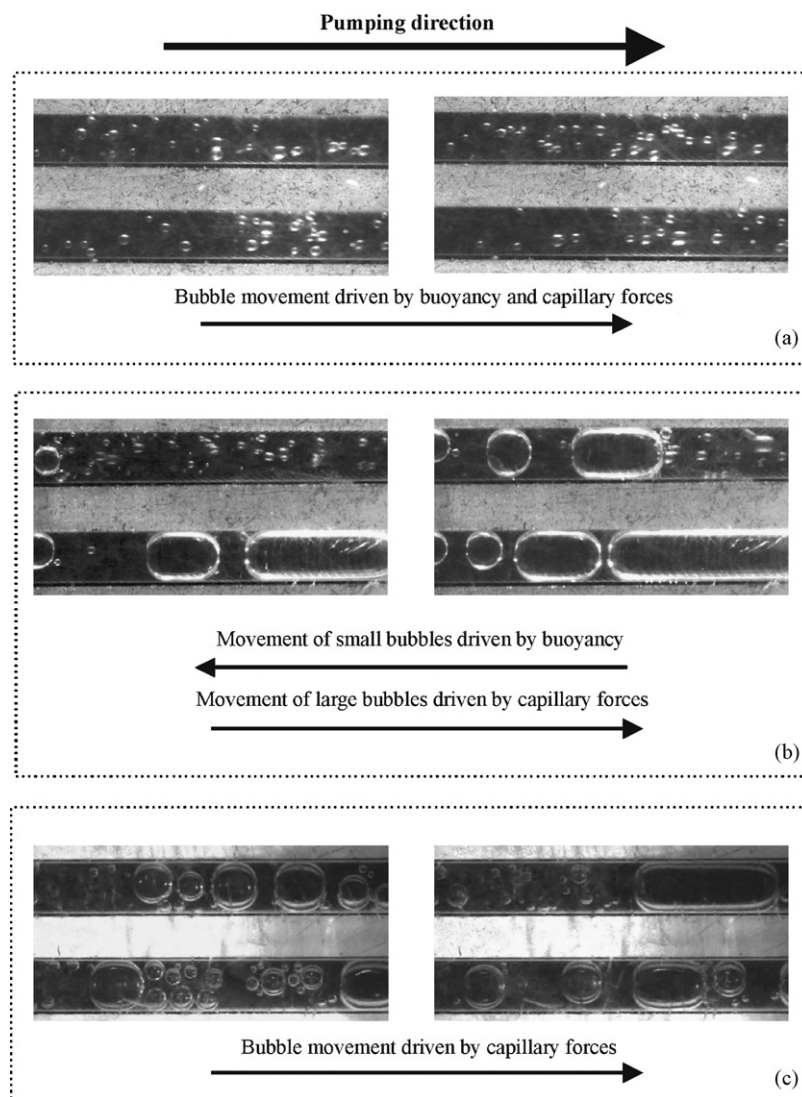


Fig. 8. Top view of moving bubbles in two parallel tapered channels of the anode flow field for different DMFC orientations at $i = 53.8 \text{ mA cm}^{-2}$. The time difference between the left and the right picture series is $\Delta t = 5.7 \text{ s}$. (a) Vertical orientation with the bubbles moving upwards. (b) Vertical orientation with the bubbles moving downwards against buoyancy forces. (c) Horizontal orientation.

increasing current densities, more liquid is dragged in the pumping direction by the numerous bubbles moving in the non-blocking mode and p_{eff} initially increases with an increasing electric load. As the load increases further, p_{eff} remains roughly constant.

The largest p_{eff} occurs at low current densities with the capillary movement of bubbles against buoyancy forces (Fig. 7 dark grey line and Fig. 8 (b)). In this orientation, small bubbles driven by buoyancy forces move in the opposite direction of the overall pumping direction. In the narrower part of the channel, these bubbles are caught either by the upper and lower channel surfaces or by a bubble that has been formed there previously. Bubbles grow from the narrow part of the channel towards the larger channel cross-section. When these bubbles exceed a certain size, the capillary forces of the bubbles that are deformed by the tapered channel walls overcome the buoyancy forces and the bubbles move in the blocking pumping mode towards the larger cross-section of the channel. Since these channel-blocking gas bubbles initially form at the inlet and then move through the complete channel, a comparatively large amount of liquid is transported by these bubbles. With increasing current densities, blocking bubbles also form in the middle of the channel, so less liquid is transported by those bubbles. As a consequence, p_{eff} decreases with an increasing electric load in the vertical DMFC

orientation when the bubbles are moving against their buoyancy forces.

In the horizontal orientation (Fig. 7 black line and Fig. 8 (c)), small bubbles remain fixed due to contact line pinning and large bubbles move in the pumping direction in the blocking mode. The size of the liquid segments enclosed by moving bubbles in the blocking mode decreases slightly with increasing current density, so that a slight decline of p_{eff} can be observed with an increasing electric load.

In all orientations, the measured mean pumping efficiency was between $p_{eff} = 7\%$ and $p_{eff} = 40\%$. The minimum required value was estimated to be at least $p_{eff} = 6\%$ when methanol crossover is already accounted for, hence, in any orientation, more methanol than critically required is delivered by the proposed passive transport mechanism. This proves the mechanism to be suitable for fuel supply in passive and portable DMFCs operating in all spatial orientations.

5.3. DMFC performance

The performance evaluation of the passive DMFC was performed at room temperature ($T = 23^\circ\text{C}$). First, as a reference experiment, measurements were performed for the horizontal orientation using

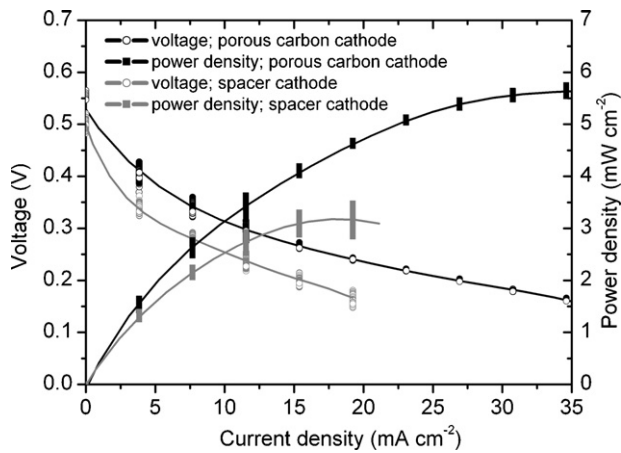


Fig. 9. Experimental results for the passive DMFC performance at ambient temperature and pressure ($p = 1 \text{ atm}$; $T = 23 \text{ }^\circ\text{C}$) for two different cathode flow fields: A simple spacer flow field compared to a cathode flow field with capillary water removal consisting of micro-structured hydrophilic porous carbon.

a cathode flow field without capillary water removal. The flow field consists of a spacer manufactured by stereo-lithography and a current collector. The polarization curve of the operating DMFC at ambient temperature and pressure is plotted in Fig. 9 (grey line). For each selected current density, measurements were performed every 10 s for galvanostatic intervals of 1 h. A break-up voltage of 150 mV was chosen in order to avoid MEA degradation at low voltages. The maximum power point (MPP) was reached at a current density of $i = 19.2 \text{ mA cm}^{-2}$ with a power output of $p = 3.2 \text{ mW cm}^{-2}$. The DMFC shows hardly any stable working points and a fluctuation of 0.7 mW was measured at the MPP, which was mainly caused by a decrease in the cell voltage over time. The unstable performance was caused by water accumulation in the cathode flow field that partially flooded the cathode and therefore hindered oxygen supply. A photograph of the passive DMFC with two enlarged sections, one showing water accumulation in the spacer cathode flow field and one showing droplet formations in the new porous carbon cathode flow field is reproduced in Fig. 10. It can be seen that in the spacer flow field, the water spreads over the cross-section of the channel (Fig. 10 left). By contrast, in the porous carbon flow field, water droplets are sucked into the bulk material as soon as they touch the side walls of the channel. Only small droplets remain (Fig. 10 right) and the channels are never blocked. The water is transported through the porous carbon and the non-woven material out of the DMFC where the water finally evaporates. In Fig. 9 (black lines), the performance of the same DMFC with the porous carbon cathode flow field implemented is depicted. The MPP is reached at a current density of $i = 35 \text{ mA cm}^{-2}$ with a power density of $p = 5.7 \text{ mW cm}^{-2}$. Comparatively low fluctuations (less than 0.3 mW) of the power density were measured for current densities between $i = 15 \text{ mA cm}^{-2}$ and $i = 35 \text{ mA cm}^{-2}$. This operation range shows a stable performance where a sufficient amount of fuel is transported to both the anode and the cathode of the DMFC.

The long-term performance of the passive DMFC for a current density of $i = 17.3 \text{ mA cm}^{-2}$ is depicted in Fig. 11 again for the two different cathode flow fields and for two different DMFC orientations. When the spacer flow field was used, the power density declined rapidly from $p = 4.3 \text{ mW cm}^{-2}$ to less than 2 mW cm^{-2} within the first 5 h of operation (Fig. 11 light grey line). The reason for the comparatively poor performance is again the water accumulation in the channels. By contrast, the porous carbon cathode flow field allows for a stable long-term performance in the same vertical DMFC orientation as in the previously performed reference experiment with the spacer cathode flow field. A continuous oper-

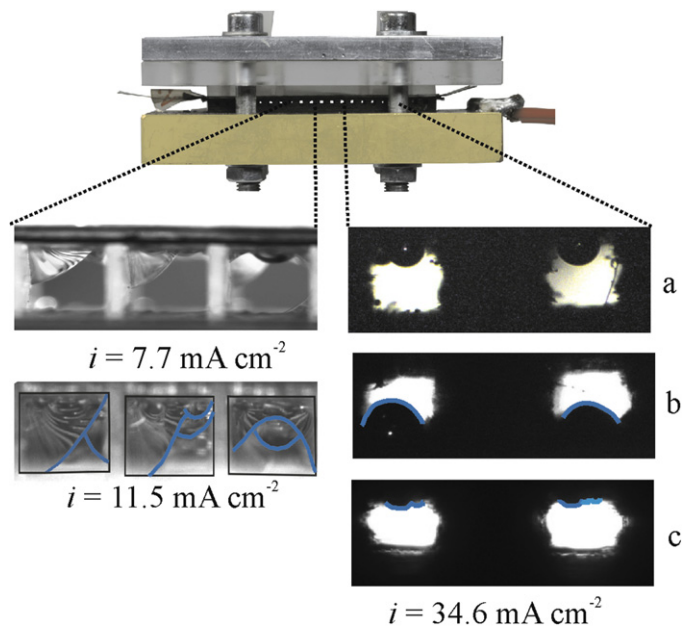


Fig. 10. Photograph of the passive DMFC with the porous carbon flow field. The enlarged segments show the water accumulation in the different cathode flow fields during the measurement of the polarization curve (Fig. 9). Left: water accumulation in the spacer flow field. Right: water formation in the porous carbon flow field with passive water removal in three different configurations: (a) horizontal, cathode facing downwards, (b) horizontal, cathode facing upwards, (c) vertical.

ation of more than 40 h was observed with a power decrease of less than 12% (Fig. 11 black line). Finally, the DMFC was tested in the most challenging position with the anode facing downwards. In this position, the buoyancy of the CO_2 gas in the water/methanol solution pushes the bubbles against the active area of the anode, and gravity does the same to water droplets at the cathode. Over the measurement period of 42 h, the power output declines from initially $p = 4.5 \text{ mW cm}^{-2}$ to $p = 3.2 \text{ mW cm}^{-2}$ (Fig. 11 dark grey line). Comparison with the vertical orientation indicates that the influence of gravity on the cell orientation is small, but still noticeable. We assume that the slightly steeper power decline in the horizontal orientation is due to an increased liquid saturation in the PTL and the formation of a water film between the catalyst layer and the PTL. When the DMFC was disassembled after this measurement, the catalyst at the cathode showed comparatively large wet spots. The increase of liquid saturation and water film formation in the horizontal orientation with the anode facing downwards may be due to an increase of the amount of water that resides in the cath-

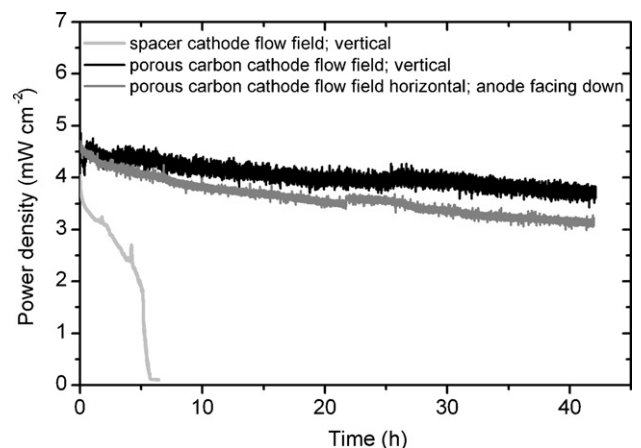


Fig. 11. Long-term power performance of the passive DMFC for the two different cathode flow fields and for two different DMFC orientations.

ode flow field channels. As a consequence, the humidity increases which reduces the diffusive water transport through the PTL and thus liquid water formation is favored in the PTL and between the PTL and the MEA. Though the fluid behavior inside the PTL and between the PTL and the MEA is not directly affected by gravity due to the small dimensions of the pores, gravity does have an influence on the water formation and transport inside the channels of the cathode flow field. Fig. 10(a–c) show the water formation inside the cathode flow field in the horizontal and the vertical orientation. It can be seen that in the vertical orientation (Fig. 10 (c)) much less water resides in the channels. The reason for the enhanced water transport in the vertical orientation is that gravity drags the water droplets forming on or emerging from the hydrophobic surface of the PTL towards the channel walls. This does not happen in the vertical orientation in which droplets that grow in the centre of the channel can reach a diameter of the channel width of 1 mm (see Fig. 10 (b)) before they touch the channel walls and become removed by capillary action. As stated above, the amount of water residing in the cathode flow field presumably influences the mass transport in the PTL and thus influences the DMFC performance. Fluid management in the PTL is not addressed in this work but might improve the performance of the passive DMFC further.

6. Conclusions

A DMFC layout concept is presented that enables the design of a passive, compact, and portable DMFC with continuous operation in all spatial orientations. The concept has been proven by constructing and testing a passive DMFC prototype. At the anode, at least 3.5 times more methanol than the stoichiometry of the methanol oxidation would require to sustain DMFC operation is transported by the supply mechanism driven by capillary movement of CO₂ bubbles. The flow rates induced by the moving bubbles closely follow the electric load, so the mechanism can be considered as self-regulating. At the cathode, oxygen is supplied by diffusion and the reaction product water is transported out of the DMFC along a continuous capillary gradient. With these features, the DMFC exhibited stable operation for more than 40 h in all orientations without the need for any external components such as pumps or valves. To further improve the performance of the passive DMFC, micro-fluid

management with respect to the porous transport layer and the interfaces between the PTL and the MEA should be considered. To further increase the energy density of the complete system, we see potential in combining a methanol dosage system and a methanol reservoir containing pure methanol as presented in [10], with the passive fuel supply concept presented and discussed in the present work.

Acknowledgements

This work was supported by the German Federal Ministry of Education and Research within Project O3SF0311B.

References

- [1] D.J. Kim, E.A. Cho, S.A. Hong, I.H. Oh, H.Y. Ha, J. Power Sources 130 (2004) 172–177.
- [2] Q. Ye, T.S. Zhao, J. Power Sources 147 (2005) 196–202.
- [3] R. Chen, T.S. Zhao, J.G. Liu, J. Power Sources 157 (2006) 351–357.
- [4] B.K. Kho, B. Bae, M.A. Scibioh, J. Lee, H.Y. Ha, J. Power Sources 142 (2005) 50–55.
- [5] Z. Guo, A. Faghri, J. Power Sources 160 (2006) 1142–1155.
- [6] B. Bae, B.K. Kho, T.H. Lim, I.H. Oh, S.A. Hong, H.Y. Ha, J. Power Sources 158 (2006) 1256–1261.
- [7] T. Shimizu, T. Momma, M. Mohamedi, T. Osaka, S. Sarangapani, J. Power Sources 137 (2004) 277–283.
- [8] Y.H. Chan, T.S. Zhao, R. Chen, C. Xu, J. Power Sources 176 (2008) 183–190.
- [9] M.A. Abdelkareem, N. Morohashi, N. Nakagawa, J. Power Sources 172 (2007) 659–665.
- [10] Y.M. Yang, Y.C. Liang, J. Power Sources 165 (2007) 185–195.
- [11] A. Faghri, Z. Guo, Appl. Thermal Eng. 28 (2008) 1614–1622.
- [12] N. Paust et al., Microfluidics and Nanofluidics, online, doi:10.1007/s10404-009-0414-9.
- [13] D.D. Meng, C.J. Kim, Lab Chip 8 (2008) 958–968.
- [14] C.Y. Chen, P. Yang, J. Power Sources 123 (2003) 37–42.
- [15] D. Langbein, Capillary Surfaces: Shape, Stability, Dynamics, in Particular Under Weightlessness, Springer, 2002.
- [16] L.C. Gao, T.J. McCarthy, Langmuir 22 (2006) 6234–6237.
- [17] M.K. Ravikumar, A.K. Shukla, J. Electrochem. Soc. 143 (1996) 2601–2606.
- [18] C. Xu, Y.L. He, T.S. Zhao, R. Chen, Q. Ye, J. Electrochem. Soc. 153 (2006) A1358–A1364.
- [19] R. Jiang, D. Chu, J. Electrochem. Soc. 151 (2004) A69–A76.
- [20] A. Theodorakakos, T. Ous, M. Gavaises, J.M. Nouri, N. Nikolopoulos, H. Yanagihara, J. Colloid Interface Sci. 300 (2006) 673–687.
- [21] S. Lister, C.R. Buie, T. Fabian, J.K. Eaton, J.G. Santiago, J. Electrochem. Soc. 154 (2007) B1049–B1058.
- [22] R. Toomey, D. Freidank, J. Rühe, Macromolecules 37 (2004) 882–887.
- [23] G.Q. Lu, C.Y. Wang, J. Power Sources 134 (2004) 33–40.
- [24] R.L. Lide, Handbook of Chemistry and Physics, CRC Press, Boca Raton, USA, 2001.